# Evaluating Seasonal Climate Forecasts from Dynamical Models over South America

JIAYING ZHANG,[a] KAIYU GUAN,[a,b,c] RONG FU,[d] BIN PENG,[a,b,c] SIYU ZHAO,[d] AND YIZHOU ZHUANG[d]

[a] *Agroecosystem Sustainability Center, Institute for Sustainability, Energy, and Environment, University of Illinois Urbana–Champaign, Urbana, Illinois*

[b] *Department of Natural Resources and Environmental Sciences, College of Agricultural, Consumer and Environmental Sciences, University of Illinois Urbana–Champaign, Urbana, Illinois*

[c] *National Center of Supercomputing Applications, University of Illinois Urbana–Champaign, Urbana, Illinois*

[d] *Department of Atmospheric and Oceanic Sciences, University of California, Los Angeles, Los Angeles, California*

(Manuscript received 6 September 2022, in final form 2 January 2023)

ABSTRACT: Seasonal climate forecasts have socioeconomic value, and the quality of the forecasts is important to various societal applications. Here we evaluate seasonal forecasts of three climate variables, vapor pressure deficit (VPD), temperature, and precipitation, from operational dynamical models over the major cropland areas of South America; analyze their predictability from global and local circulation patterns, such as El Niño–Southern Oscillation (ENSO); and attribute the source of prediction errors. We show that the European Centre for Medium-Range Weather Forecasts (ECMWF) model has the highest quality among the models evaluated. Forecasts of VPD and temperature have better agreement with observations (average Pearson correlation of 0.65 and 0.70, respectively, among all months for 1-month-lead predictions from the ECMWF) than those of precipitation (0.40). Forecasts degrade with increasing lead times, and the degradation is due to the following reasons: 1) the failure of capturing local circulation patterns and capturing the linkages between the patterns and local climate; and 2) the overestimation of ENSO's influence on regions not affected by ENSO. For regions affected by ENSO, forecasts of the three climate variables as well as their extremes are well predicted up to 6 months ahead, providing valuable lead time for risk preparedness and management. The results provide useful information for further development of dynamical models and for those who use seasonal climate forecasts for planning and management.

SIGNIFICANCE STATEMENT: Seasonal climate forecasts have socioeconomic value, and the quality of the forecasts is important to their applications. This study evaluated the quality of monthly forecasts of three important climate variables that are critical to agricultural management, risk assessment, and natural hazards warning. The findings provide useful information for those who use seasonal climate forecasts for planning and management. This study also analyzed the predictability of the climate variables and the attribution of prediction errors and thus provides insights for understanding models' varying performance and for future improvement of seasonal climate forecasts from dynamical models.

KEYWORDS: Atmospheric circulation; Climate prediction; Dynamical system model; Extreme events; Forecast verification/skill; Seasonal forecasting

## 1. Introduction

Seasonal climate forecasts provide valuable information for early warnings, risk assessment, and decision-making processes in multiple sectors, including but not limited to disaster management, water resources, agriculture, energy, and public health (Thomson et al. 2006; Clements et al. 2013; National Research Council 2016; Andersson et al. 2020; Orlov et al. 2020; White et al. 2022). Take the agriculture sector as an example: seasonal climate forecasts have been used to support operational decisions on crop management (selection of crops, timing of planting and harvest), irrigation scheduling, and product marketing and trading (Clements et al. 2013; Ceglar and Toreti 2021; White et al. 2022). As seasonal climate forecasts continue increasing their socioeconomic potentials, several meteorological forecast services around the world, such as the European Centre for Medium-Range Weather Forecasts (ECMWF), the Meteorological Office of the United Kingdom, and the United States' National Centers for Environmental Prediction (NCEP), are providing routine operational seasonal forecasts at regional and global scales. However, the quality of those forecasts varies with dynamical models, variables of interest, and geographical locations, among other factors, and inaccurate forecasts may even be harmful to end users (Ziervogel et al. 2005). Therefore, the quality of the climate forecasts needs to be thoroughly evaluated.

There are numerous studies evaluating the quality of monthly and seasonal climate forecasts (Jia et al. 2015; Ogutu et al. 2017; Johnson et al. 2019; Gubler et al. 2020; Ehsan et al. 2021; Klingaman et al. 2021; Calì Quaglia et al. 2022). Almost all the existing studies focused on forecasts of precipitation or/and air temperature, two of the most important climate variables that are essential for agricultural planning and are indicators of natural disasters such as heat waves, floods, and droughts. Another variable, vapor pressure deficit (VPD), is also essential for agricultural planning and risk assessment (Lobell et al. 2014;

Supplemental information related to this paper is available at the Journals Online website: https://doi.org/10.1175/JHM-D-22-0156.s1.

*Corresponding authors*: Kaiyu Guan, kaiyug@illinois.edu; Jiaying Zhang, zhjiay5@illinois.edu

DOI: 10.1175/JHM-D-22-0156.1

Peng et al. 2018) and an indicator of plant water stress (Zhang et al. 2021a,b), droughts (Kimm et al. 2020; Zhou et al. 2020), and wildfires (Mueller et al. 2020; Zhuang et al. 2021) and thus also deserves attention. VPD is the difference between the moisture in the air and the moisture the air can hold at saturation; it describes air humidity and evapotranspiration and regulates plant growth and functioning (Yuan et al. 2019; Grossiord et al. 2020). VPD forecasts are not available for most seasonal forecast models (such as those participating in the North American Multi-Model Ensemble) except for those who join the Copernicus Climate Change Service [i.e., ECMWF, the Met Office (UKMO), Météo-France (MF), Deutscher Wetterdienst (DWD), Centro Euro-Mediterraneo sui Cambiamenti Climatici (CMCC), NCEP, and Japan Meteorological Agency (JMA)], not to mention the evaluations of the forecasts.

Climate variables at monthly and seasonal scales are strongly influenced by El Niño–Southern Oscillation (ENSO), an oceanic and atmospheric circulation teleconnection pattern. The predictability of ENSO is argued to be the main source of predictability of the climate at monthly and seasonal time scales for many regions over the globe (Manzanas et al. 2014). Dynamical models have reliable skills to predict ENSO with months ahead but the prediction skill for climate variables, especially precipitation, is less promising (Johnson et al. 2019). The skill of climate forecasts depends also on the skill of forecasts of local circulation patterns and the forecast linkages between the patterns and the climate. A recent study showed that ECMWF failed to predict the North American monsoon precipitation but successfully forecasted the local circulation patterns (Prein et al. 2022), which were then used to estimate the precipitation accurately (Prein et al. 2022). Therefore, understanding the forecast skill of local circulation patterns can help identify model deficiencies and provide information for future model improvement.

South America plays an increasingly important role in global crop production. Brazil has exceeded the United States in soybean production and become the largest producer in recent years and is likely to be the world leader in soybean production in the next decade (Colussi and Schnitkey 2021). In addition, Brazil is the largest producer of sugarcane (the most produced crop product), and its annual production accounted for 13% of world production in 2000 and increased to 40% in 2019 (FAO 2021). Brazil is also the second largest producer of cattle, which relies heavily on pasture and grassland. However, Brazil's grass and crop production depends on the climate condition: yields decline in dry and hot years with unusually low precipitation during the early stages of crop development (Rattis et al. 2021). Therefore, climate forecasts with months ahead are of vital importance to agricultural planning and risk management of the regions.

Seasonal forecasts of temperature and precipitation in South America from dynamical models have been widely evaluated (e.g., Bombardi et al. 2018; Andrian et al. 2023; Ferreira et al. 2022). The seasonal forecasts of temperature are generally better than those of precipitation (Andrian et al. 2023; Ferreira et al. 2022); temperature has high predictability over northern South America and moderate predictability over higher latitudes, while precipitation has moderate predictability over northeastern Brazil and southeastern South America (Andrian et al. 2023). The predictability of summer precipitation over northern and southeastern South America is from ENSO, which modulates its dominant interannual variability (Bombardi et al. 2018). However, the prediction performance does not solely stem from ENSO, but also from local processes (Gubler et al. 2020).

Similar to other regions in the world, the climate in South America is influenced by the ENSO teleconnection, commonly represented by the Niño-3.4 index (Cai et al. 2020). During an El Niño event, the positive sea surface temperature (SST) anomaly in the equatorial eastern Pacific decreases the east–west SST gradient and hence weakens the Walker circulation (Gill 1980), resulting in a warmer and drier condition over the equatorial eastern South America and a cooler and rainier condition over southeastern South America through Rossby wave teleconnections (Ghil and Mo 1991; Cai et al. 2020). The impact of ENSO on South America climate is modulated by other large-scale oceanic and atmospheric patterns, such as Indian Ocean dipole (IOD) mode (Chan et al. 2008), Southern Annular Mode (SAM) (Gillett et al. 2006; Vera and Osman 2018), and Pacific–South American (PSA) pattern (Irving and Simmonds 2016). These large-scale patterns affect local circulations, such as trade winds and the South America low-level jet (SALLJ) (Boers et al. 2014; Montini et al. 2019). Specifically, trade winds with moist air from the tropical Atlantic are blocked by the Andes after reaching the Amazon basin and then deflected to the south (forming the SALLJ), facilitating the development of mesoscale convective systems, and contributing to precipitation in southeast South America (Salio et al. 2007; Boers et al. 2014). Therefore, a high-performance forecast of trade winds and the SALLJ may help to forecast climate variables, such as precipitation and VPD, in South America.

This study addressed two scientific questions: 1) How do dynamical models perform on seasonal time scales? 2) How could dynamical models potentially improve their predictions? To answer the first question, we evaluated the ability of dynamical models in capturing the spatial and temporal patterns of three important climate variables (temperature, precipitation, and VPD). The quality of the forecasts was evaluated for each month with 1–6-month lead time for the major croplands over South America. We also evaluated the models' ability in predicting extremes associated with the climate variables. To answer the second question, we analyzed the linkages between potential predictors, i.e., global and local circulation patterns, and the local climate and quantified the contribution of prediction errors of circulation patterns to the prediction errors of the climate variables.

## 2. Data and methods

### *a. Evaluated variables*

We evaluate three climate variables, i.e., VPD, temperature, and precipitation, over the major crop production region of South America (66°–40°W, 42°–0°S) (Fig. 1b) and three

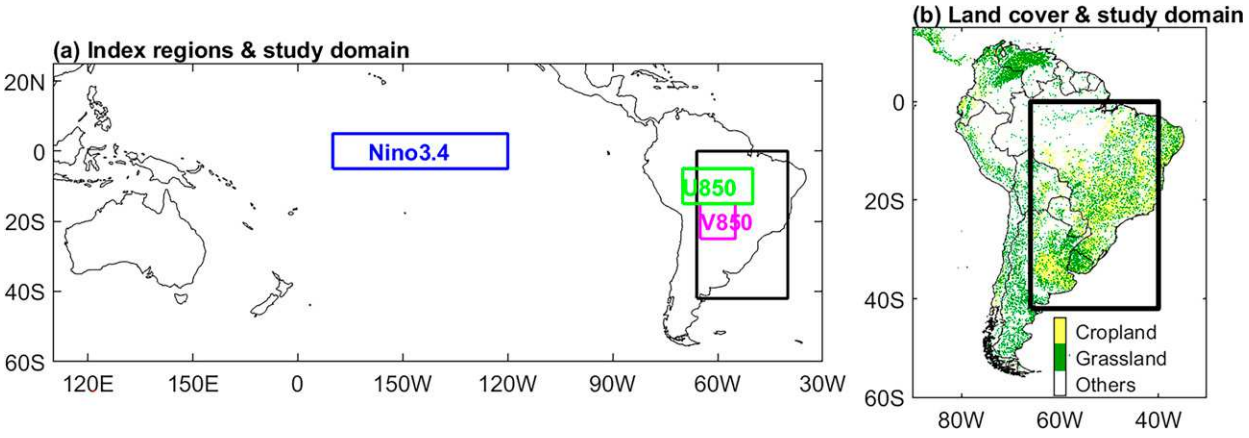


FIG. 1. Land cover and the study domains. (a) The study domain (66°–40°W, 42°–0°S) and the region of the three indices: Niño-3.4 (170°–120°W, 5°S–5°N), V850 (65°–55°W, 25°–15°S), and U850 (70°–50°W, 15°–5°S). (b) Three land cover types in South America and the study domain. The original land cover data are from GLOBCOVER 2009 (ESA 2010). Regions that contain croplands in the original land cover data are grouped into "Cropland"; regions that contain grasslands are grouped into "Grassland"; regions that are a mosaic of croplands and grasslands are grouped into Cropland if croplands account for more than 50% and Grassland otherwise; and the rest is grouped into "Others."

circulation patterns, i.e., ENSO, northerly moisture transport associated with the SALLJ, and easterly moisture transport associated with trade winds, that affect the local climates at a monthly scale. VPD is calculated as the difference between the saturated vapor pressure given air temperature ($T$; °C) and the actual vapor pressure, and thus it describes the dryness of the air. The higher the VPD value, the drier the atmosphere. The saturated vapor pressure is calculated as follows:

$$\mathrm{svp}(T) = 6.108 \times \exp\left(\frac{17.27 \times T}{T + 237.3}\right). \quad (1)$$

To overcome the underestimation of VPD due to temporal aggregation (Allen et al. 1998), monthly mean VPD is calculated as

$$\mathrm{VPD} = \frac{[\mathrm{svp(Tmn)} + \mathrm{svp(Tmx)}]}{2} - \mathrm{svp(Dmean)}, \quad (2)$$

where Tmn and Tmx are the monthly mean of daily minimum and maximum air temperatures, respectively, and Dmean is the monthly mean dewpoint temperature. The ENSO phenomenon is represented by the Niño-3.4 index, which is the SST average over 170°–120°W, 5°S–5°N. Northerly moisture transport associated with the SALLJ is represented by the V850 index defined as the 850-hPa meridional wind averaged over 65°–55°W and 25°–15°S (Wang et al. 2004). Easterly moisture transport associated with trade winds is represented by the U850 index defined as the 850-hPa zonal wind averaged over 70°–50°W, 15°–5°S (Yin et al. 2014). We choose the three indices because the local climate over South America is influenced mostly by these indices (Fig. S1 in the online supplemental material). The location of the study domain and the indices are shown in Fig. 1a. Variables and indices are standardized against the mean and standard deviation of each month during 1994–2016 (corresponding to the hindcast period of the dynamical models, see the next section).

### b. Forecasts from dynamical models

The 1–6-month-lead forecasts of monthly air temperature and total precipitation are obtained and VPD calculated for five models from the Copernicus Climate Change Service (C3S) Climate Data Store (CDS) (ECMWF, UKMO, MF, DWD, and CMCC) (https://cds.climate.copernicus.eu/). The other two models in the CDS are not included (NCEP and JMA) as they do not have matched variables. Forecasts of the three indices (Niño-3.4, V850, U850) are calculated only for the ECMWF model because it outperforms the others. The forecasts have been initialized since January 1993 and the predictions were made for each day and up to 6 months after the initialization. The predictions between 1993 and 2016 are referred to as hindcasts and those after 2016 are referred to as forecasts (we will not distinguish hindcast and forecast hereafter, but only the hindcast period and forecast period). Since the first initialization date is in January 1993, the 2–6-month-lead predictions for January 1993 are not available, and so for 3–6-month-lead predictions for February 1993, etc. As the predictions in 1993 and those in the forecast period are not always available (Table S1), we focus on the hindcast period between 1994 and 2016 in this study. The forecasts have global coverage with 1° spatial resolution. Table S1 lists the details of the models and further details of the dynamical models are referred to the Copernicus Climate Change Service.

### c. Benchmark data

Monthly temperature and VPD from ECMWF Reanalysis v5 (ERA5) (Muñoz Sabater 2019b) are used to benchmark temperature and VPD forecasts. The daily minimum and maximum 2-m air temperatures used to calculate the monthly VPD are from the hourly ERA5 data (Muñoz Sabater 2019a)

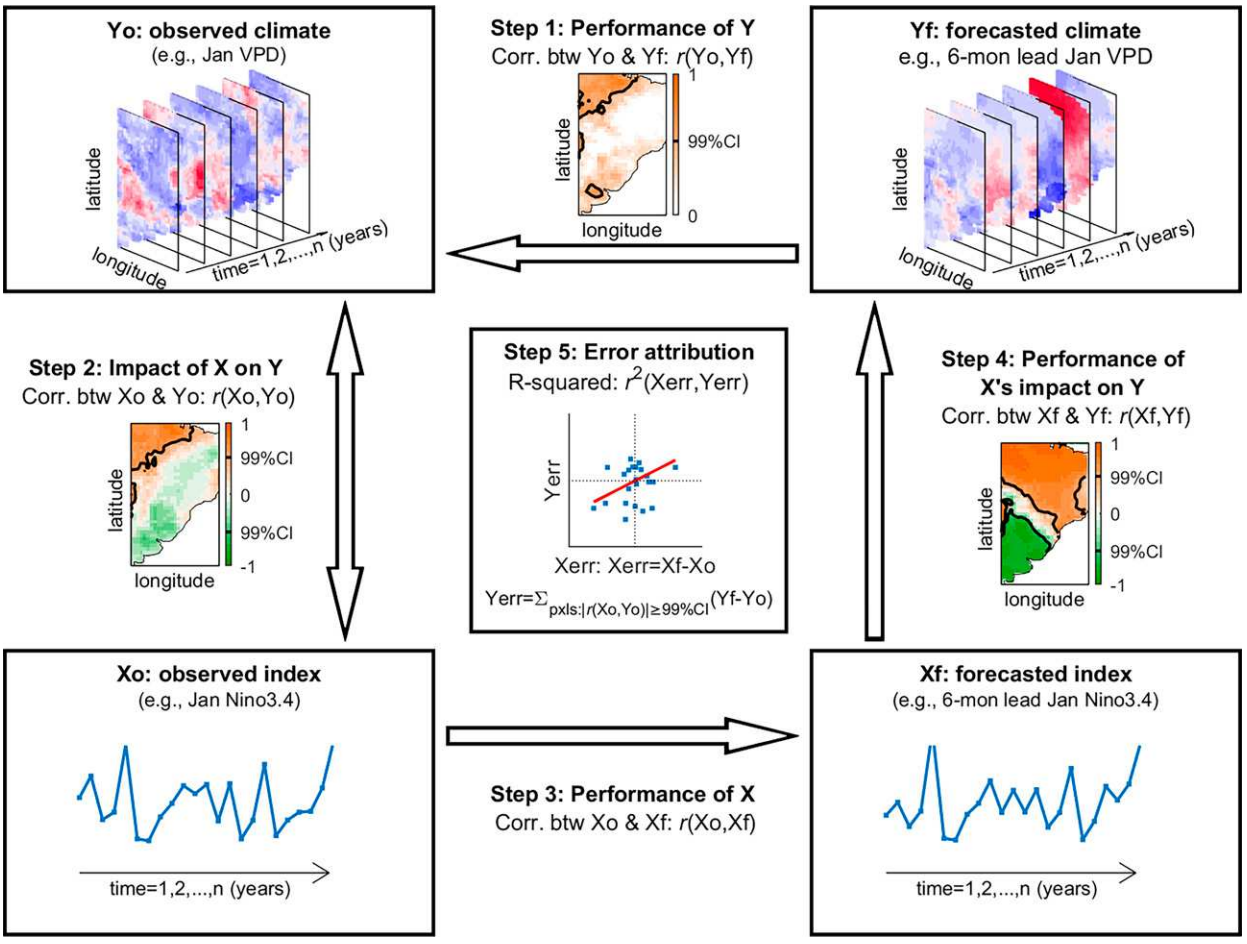


FIG. 2. Evaluation framework. Observed and forecasted climate variables are referred to as Yo and Yf, respectively; and observed and forecasted indices are referred to as Xo and Xf, respectively. In step 1, we evaluate models' ability in predicting climate variable $Y$ through correlation coefficient ($r$) between observation and model forecasts [$r$(Yo, Yf)]. In step 2, we evaluate the observed effect of index $X$ on $Y$ [$r$(Xo, Yo)]. In steps 3 and 4, we evaluate the model's performance in predicting index $X$ [$r$(Xo, Xf)] and in capturing the linkage between $X$ and $Y$ [$r$(Xf, Yf)], respectively. In step 5, we show how much of the climate variable errors (Yerr) were attributed to index errors (Xerr) [$r^2$(Xerr, Yerr)], where the errors are defined as the difference between model forecasts and observations. For Yerr, it is the average of errors over the pixels of high impact from $X$, defined as $r$(Xo, Yo) is significant at 99% confidence level via Student's $t$ test as outlined by the thick black line in step 2.

using the daily statistics calculator application provided by the Copernicus CDS, and then aggregated to get monthly values. The spatial resolution of the ERA5 data used in this study is 1° × 1°. Precipitation (mm day$^{-1}$) data used to benchmark the precipitation forecasts are from CPC daily precipitation with 0.25° spatial resolution. Missing values of daily precipitation (20070226, 20020701, 20050728) were filled with the values in the previous day, and then the daily data were aggregated to monthly mean data. The CPC precipitation is linearly interpolated into 1°. The Niño-3.4 index is obtained from the NOAA Physical Sciences Laboratory (PSL) website; the V850 and U850 indices are calculated from the ERA5 monthly data.

### *d. Evaluation framework and metrics*

To simplify the notations, we refer to climate variables as $Y$ and indices as $X$; those from observations as Yo and Xo and those from forecasts as Yf and Xf. Figure 2 shows the framework for evaluating dynamical model forecasts with five steps. Step 1 evaluates models' performance in predicting climate variables of interest, which is represented by the correlation between forecasts and observations [$r$(Yo, Yf)]. To understand the predictability of the climate variables, steps 2–4 evaluate potential predictors (e.g., circulation patterns) that affect local climates. Specifically, step 2 evaluates the observed linkages between potential predictors and the climate variables, which are represented by the correlation between climate variables and indices from the observations [$r$(Xo, Yo)]. Step 3 evaluates the models' performance in predicting the predictors and step 4 in capturing the linkages, which are represented by the correlation between forecasts and observations for the indices [$r$(Xo, Xf)] and the correlation between climate variables and indices from forecasts [$r$(Xf, Yf)], respectively.

Last, to investigate the source of prediction errors of the climate variables and thus to help future model developments, step 5 quantifies the contribution of predictor errors to climate variable errors, which is represented by the coefficient of determination between the errors of climate forecasts and the errors of indices forecasts [$r^2$(Xerr, Yerr)]. The errors are calculated as the difference between forecasts and observations, and for the spatially distributed climate variables, the errors (Yerr) are the averages across the grid points that are significantly affected by the index (Xo), that is, $r$(Xo, Yo) exceeds the 99% confidence level. Therefore, the $r^2$(Xerr, Yerr) explains the contribution of the index error to the climate variable error in the corresponding regions.

Three verification metrics are used to evaluate the performance of forecasts compared to the benchmark data: Pearson correlation coefficient ($r$; CC), Heidke skill score (HSS), and root-mean-square error (RMSE); the coefficient of determination ($r^2$) metric is used to quantify the variance of one variable explained by another, or the attribution of one variable to another. CC is used to measure the performance on spatial or temporal patterns, and it is verified by Student's $t$ test given the sample size. RMSE measures the random error of the predictions, since all variables are standardized, the RMSE measures the error in the scale of the standard deviation of the variable and thus a RMSE of 1 can be used as a threshold to distinguish the good and poor performance in terms of errors. To compare the RMSE with the climatology of the variable, we define rRMSE (%) where we multiply the RMSE with the standard deviation of the observations and then divide it by the climatology. Since the variables are standardized, this way of calculating rRMSE is the same as rescaling the forecasts such that the forecasts and observations have the same mean and standard deviation, then calculating the RMSE between the rescaled forecasts and the observations, and then normalizing the RMSE by the climatology. Note that model bias is removed before evaluation as the variables are standardized. HSS is used to quantify the detection skill of the forecasts on the sign (positive or negative) of the standardized variable (Zhao et al. 2021, 2023),

$$\mathrm{HSS} = \frac{H - E}{N - E}, \tag{3}$$

where $N$ is the total number of samples of a variable, and $H$ and $E$ are the total and expected number of the correct predictions of the sign of the standardized variable, and $E$ has an expected value of $N/3$ for a random forecast. The value of HSS ranges from $-0.5$ to 1 and a score of 1 ($-0.5$) indicates a perfect (perfectly incorrect) prediction, and a value of 0.5 is commonly used as a threshold to distinguish the good and poor detection skill.

As the response of the climates to the circulation patterns varies spatially in the study domain, we group pixels with similar temporal variability into clusters using hierarchical clustering analysis. Specifically, we calculate the Euclidean distance with a Ward's linkage (Ward 1963; Zhao et al. 2017) between any two clusters, and clusters with small Euclidean distances can merge. We choose the Euclidean distance of 5 as the threshold for merging and the consequent number of clusters is retained. A large threshold may lead to too few clusters (fails to distinguish the differences) while a small threshold may lead to too many clusters (fails to group the similarities), and a choice of 5 gives a reasonable number of clusters (2–5) for each monthly climate variable as shown in the supplemental material (supplemental videos S1, S2, and S3).

Aside from the verification metrics, we also calculate several indices describing the extreme of a year. An extreme wet year is defined such that the cumulative density (i.e., the proportion of grids that meet a certain criterion) of VPD being less than $-1$ [CD($Y < -1$)] or the cumulative density of precipitation being greater than 1 [CD($Y > 1$)] is as large as possible, and vice versa for an extreme dry year. Note that all variables are standardized and thus a value of 1 indicates one standard deviation from the mean (or climatology). Extreme hot or extreme cold years can be defined similarly with respect to the variable temperature. Since the study domain is too large to have a strictly extreme wet (or dry) situation for the whole domain, that is, one part of the domain may be extremely wet, but the other part could be extremely dry, a year could be both an extremely wet year for one part of a domain and an extremely dry year for the other part of the domain. To describe the generality of the extreme situation of a year, we calculate the cumulative density of extremes, the cumulative density of a variable being either less than $-1$ or greater than 1 [CD($|Y| > 1$)], and thus the cumulative density of extremes describes the proportion of domains being extreme (either extremely wet or extremely dry).

## 3. Results and discussion

### a. *Overall performance of climate forecasts*

Among the three climate variables, temperature has the best forecasts in terms of the correlation with observations (Fig. 3), the HSS detection score (Fig. S2), and the RMSE (Fig. S3). Precipitation forecasts have the lowest correlation and HSS detection score, and the highest RMSE. VPD has intermediate quality compared to temperature and precipitation. Since VPD could be more important to plant growth than precipitation (Voelker et al. 2014), and the forecasts of VPD have better agreement with observations than precipitation forecasts, the VPD forecasts from dynamical models could be more useful than precipitation forecasts for ecological and agricultural applications.

The quality of the forecasts also varies with target month and lead time. During October–May, corresponding to the growing season of soybean in South America, the forecasts of VPD have a correlation of 0.53 (average for all models and the eight months between October and May) for the 1-month-lead prediction but decreased to 0.26 for the 6-month-lead prediction; while the forecasts during June–September decreased from 0.47 with 1-month lead to 0.14 with 6-month lead. The higher performance during the growing-season months than

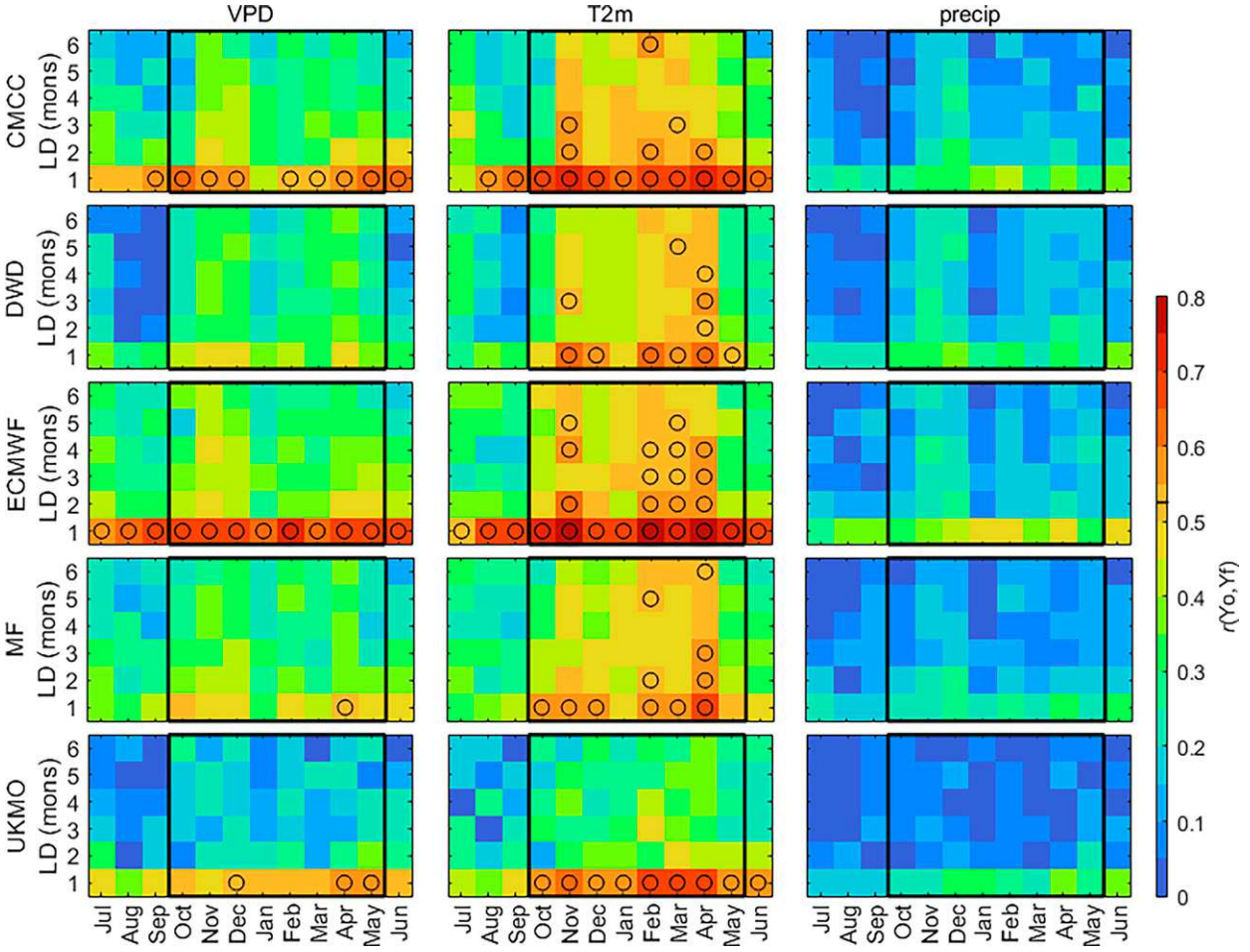


FIG. 3. The correlation coefficient ($r$) between observed and forecasted climate variables (VPD, T2m, and precip) in each month with each lead time from the five dynamical models (CMCC, DWD, ECMWF, MF, and UKMO). The correlation coefficients are calculated from the time series between 1994 and 2016 for each pixel over the region (66°–40°W, 42°S–0) (as in step 1 in Fig. 2). The figure shows the spatial average of the coefficients over all pixels. The 99% confidence level of the correlation coefficient of the time series of a single pixel is marked in the color bar and the coefficients that exceed the confidence level are circled in the figure. The black box in each panel indicates the growing season (October–May) of soybean in South America.

that during the non-growing-season months is also observed for temperature (0.63 versus 0.48 for 1-month-lead predictions) and for precipitation (0.31 versus 0.28 for 1-month-lead predictions), consistent with a previous study that found higher forecast skills in austral summer (December–February) and autumn (March–May) than in austral winter (June–August) (Andrian et al. 2023).

The ECMWF model has the best quality among the five dynamical models evaluated, consistent with a previous study that compared ECMWF with other models at a subseasonal scale (Klingaman et al. 2021). The 1-month-lead VPD prediction from ECMWF has a correlation of 0.66 averaged for growing-season months, while that correlation is at least 15% smaller for other models (0.56, 0.42, 0.46, and 0.53 for CMCC, DWD, MF, and UKMO, respectively). The 1-month-lead prediction for temperature and precipitation from the ECMWF model has a correlation of 0.74 and 0.41, respectively. Since ECMWF has the best quality among the models, we will focus on the forecasts from the ECMWF model in the rest of the evaluations.

### b. *Spatial heterogeneity of performance*

The quality of climate forecasts varies spatially (Fig. 4, Figs. S4–S11). For VPD forecasts, even though the overall performance of the 1-month-lead predictions are good ($r > 0.53$; $p < 0.01$) for each month (Fig. 3), the forecasts over the eastern Central Andes have low correlations ($r < 0.53$; $p > 0.01$) with observations and high errors (RMSE $> 1$ and rRMSE $> 25\%$) from October to April, and the low performance is also observed over southern Brazil from May to August (Fig. 4 and Figs. S4, S5). Similarly, although the overall performance of VPD forecasts is poor when the lead time is longer than 2 months (Fig. 3), the forecasts over northern Brazil have correlations ~0.7, RMSEs ~0.7, and rRMSEs ~10% from October to April even for 6-month-lead predictions (Fig. 4 and Figs. S4, S5); and the same for regions of Uruguay and eastern Argentina from October to January.

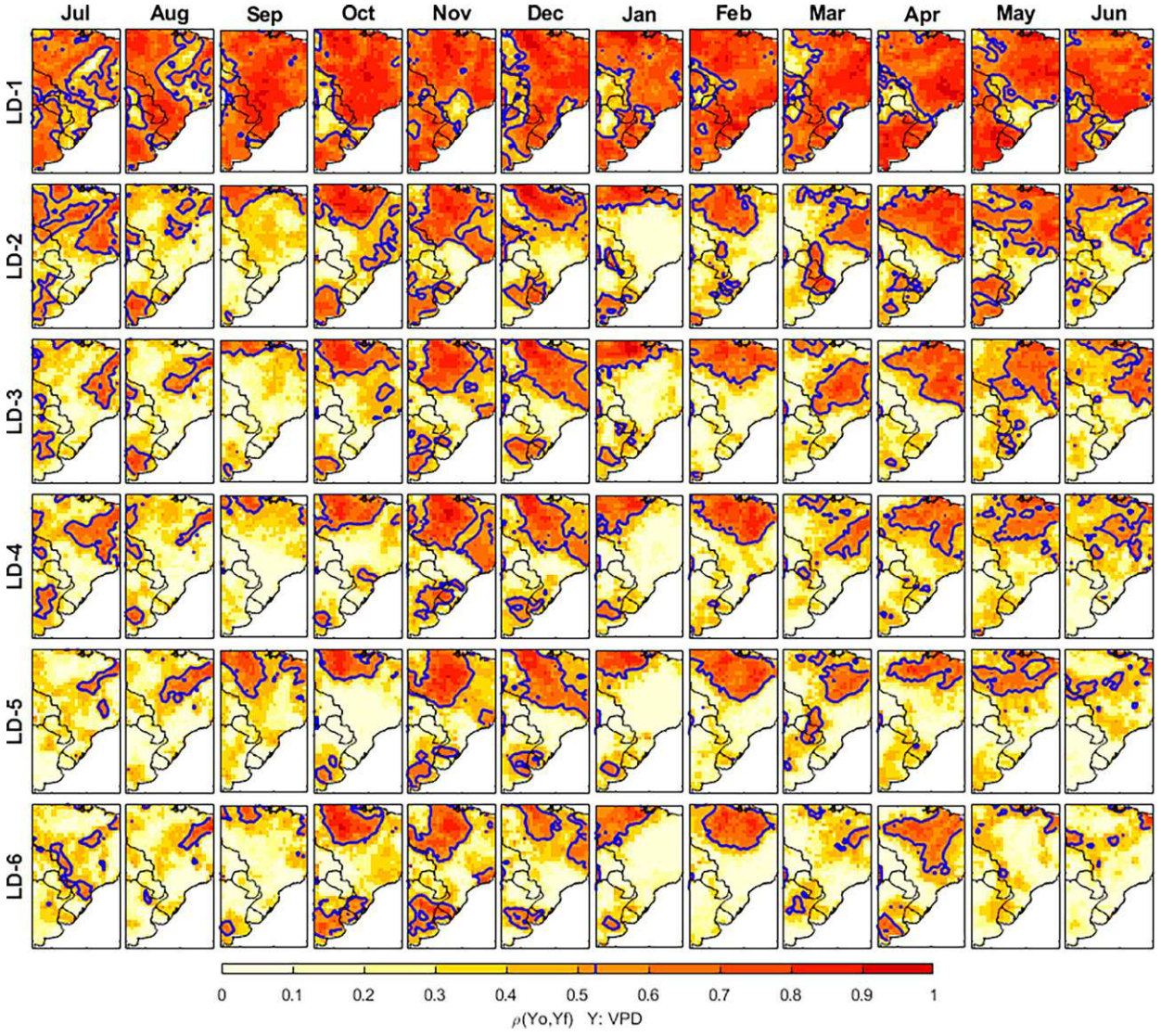


FIG. 4. The spatial map of the correlation coefficient ($r$) between observed and forecasted VPD in each month with each lead time [LD-1–LD-6 for 1–6-month lead, respectively]. The correlation coefficients are calculated from the time series between 1994 and 2016 for each pixel. The 99% confidence level of the correlation coefficient is outlined with thick blue lines.

For precipitation forecasts, the 1-month-lead prediction over northeastern Brazil, Uruguay, and eastern Argentina is significantly correlated with observations in the growing season (Fig. S6). The quality of the forecasts holds even when the prediction is conducted 6 months ahead for regions over Uruguay and eastern Argentina in November and December (Figs. S6–S8). Temperature forecasts are better than both VPD forecasts and precipitation forecasts (Figs. S9–S11). The temperature forecasts have CC exceeding 0.9, RMSE less than 0.5, and rRMSE less than 0.5% for some parts of northern Brazil in the growing season with a 1-month lead, and the CC remains larger than 0.6 with longer lead times. Over the southern part of South America, however, the temperature forecasts have low CCs (<0.3) and high RMSEs (>1) when the lead time is longer than 2 months (Figs. S9–S11). The spatial variation of the performance of temperature and precipitation forecasts is consistent with previous findings (Andrian et al. 2023; Ferreira et al. 2022).

### c. *Performance of extreme events*

Accurate prediction of extreme events, such as extreme wet and extreme dry events, is important to risk preparedness and assessment, and thus in this section, we evaluate ECMWF's ability to predict extreme events. Based on January VPD observations, 1997 and 2008 are selected as two extreme wet years and 2006 and 2015 two extreme dry years (Fig. S12). The observations and forecasts of January VPD in those extreme years are shown in Fig. 5. Even though the ECMWF model has a hard time capturing the location and magnitude of the extremes (VPD > 1 or VPD < −1), the forecasts agree

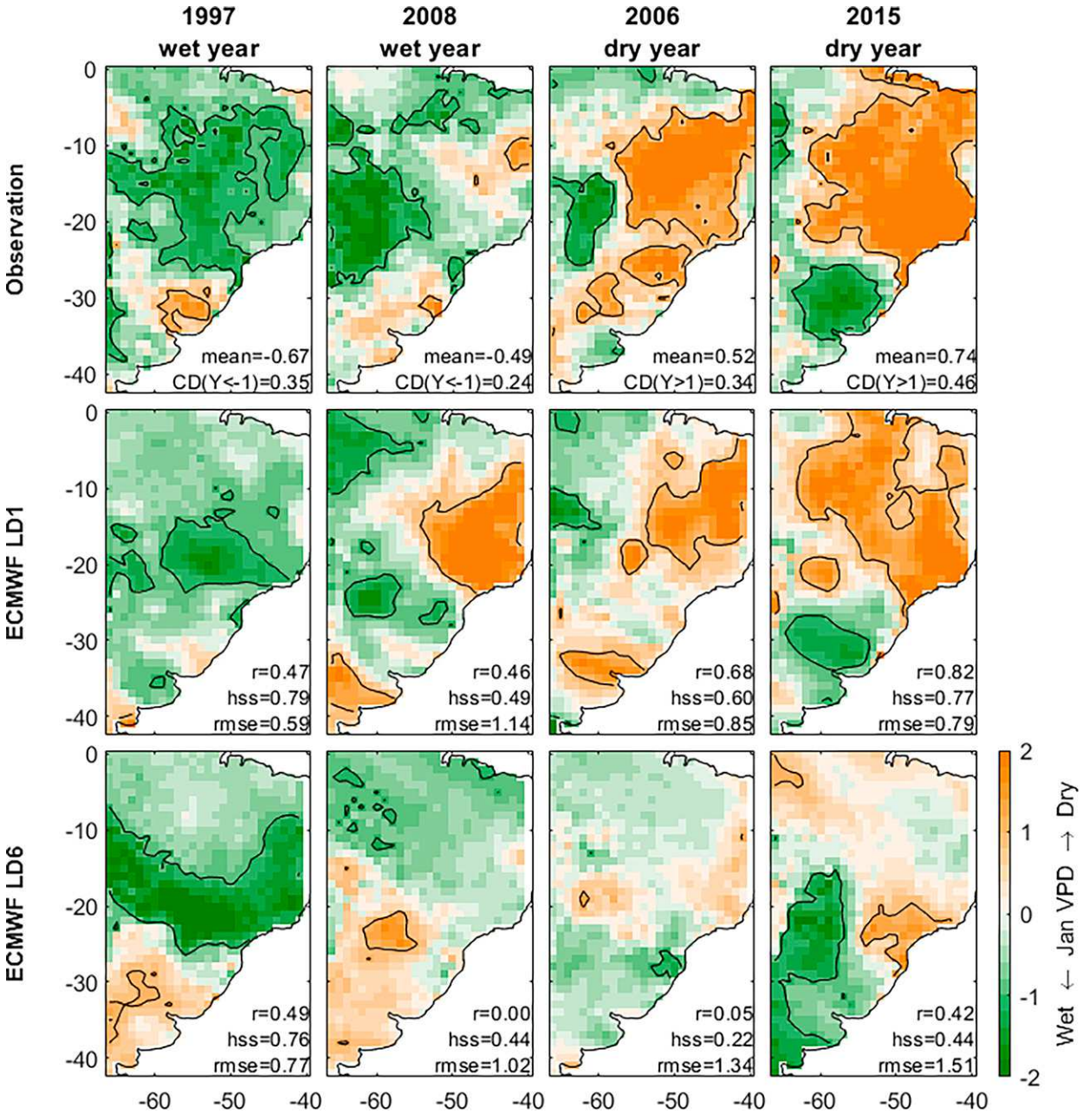


FIG. 5. Observed and forecasted January VPD in two wet years (1997 and 2008) and two dry years (2006 and 2015). The forecasts are 1-month-lead (LD1) and 6-month-lead (LD6) predictions from the ECMWF model. For observations, the domain mean value and the cumulative density of VPD smaller than $-1$ [CD($Y < -1$)] are listed for wet years; the domain mean and the cumulative density of VPD larger than 1 [CD($Y > 1$)] are listed for dry years. For forecasts, the correlation coefficient ($r$), HSS, and RMSE against the corresponding observations are listed. Black lines indicate the contours of 1 and $-1$.

well with observations in terms of the spatial pattern in the wet or dry years, especially for the 1-month-lead prediction: the correlations with observations are ~0.5 for the two wet years and ~0.7–0.8 for the two dry years, and the HSS detection scores are between ~0.5 and 0.8. The quality of the 6-month predictions decreased significantly compared to the 1-month predictions for the wet year 2008 and the dry year 2006, but still has a correlation of ~0.4 for the wet year 1997 and the dry year 2015. The performance for extreme years based on precipitation (Fig. S13) is similar to the performance of extremes based on VPD, while temperature is well predicted in extreme years even with a 6-month lead (Fig. S14).

Note that an extreme wet year does not mean extreme wet conditions for the whole domain, as a part of the domain could be extremely dry; the same applies to an extreme dry

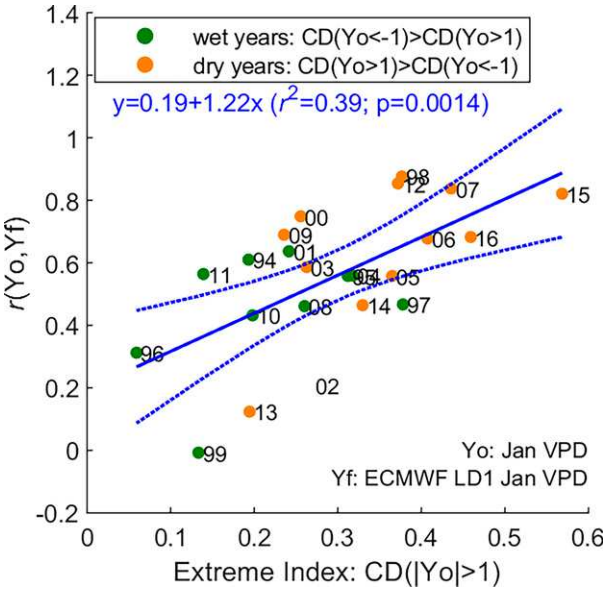


FIG. 6. Model performance of January VPD vs the index of extreme for each year. Model performance is quantified by the correlation coefficient between forecast and observed January VPD [$r$(Yo, Yf)], and the forecasted January VPD is 1-month lead predictions from ECMWF. The extreme index of a year is defined as the cumulative density (CD) of the standardized variable value exceeding +1 or −1 among the pixels in the study domain ($|\text{Yo}| > 1$). If the cumulative density of the positive part [CD(Yo > 1)] is larger than that of the negative part CD(Yo < −1), then the year is defined as a dry year in this figure, and a wet year otherwise. The linear relationship between $r$(Yo, Yf) and the extreme index is estimated, and the $r^2$ and $p$ value metrics for the relationship are calculated. The solid line is the linear regression, and the dashed lines are the 95% confidence bounds for the fitted regression.

year (Fig. 5). To quantify the overall extreme situation of a year, an extreme index, defined as the cumulative density of both extremely wet and extremely dry ($|Y| > 1$), is calculated. The regression of the quality of 1-month-lead January VPD forecasts on the extreme index has a coefficient of 1.22 ($p = 0.0014$) (Fig. 6), suggesting that the forecasts are better in more extreme years. Figure 6 also shows that the forecasts of 1-month-lead January VPD in dry years, when the dry region is larger than the wet region, have higher correlations with observations than those in wet years, when the wet region is larger than the dry region. Although this relationship between forecast quality and extreme index does not hold for every variable, it holds for monthly VPD in January–May and September–October; monthly temperature in January, April, and September; and monthly precipitation in December–April for the 1-month-lead predictions from the ECMWF model (Fig. S15).

### d. *Performance in relation to oceanic and atmospheric patterns*

As shown in Figs. 4 and 5, the climate variables have spatial variations, and those spatial variations are a result of the impact of oceanic and atmospheric circulation patterns, such as ENSO (Cai et al. 2020), northerly moisture transport associated with SALLJ (Montini et al. 2019), and easterly moisture transport associated with trade winds (Yin et al. 2014). Moreover, the occurrence of ENSO is the major cause of extreme wet/dry and cold/hot events (Pepler et al. 2015; Hao et al. 2018; Cai et al. 2020). Therefore, in this section, we evaluate the performance of the ECMWF model in capturing the circulation patterns (Fig. 7) and in capturing the linkages between the patterns and the climate variables (Fig. 8).

The ENSO signal, represented by the Niño-3.4 index, is well captured by the ECMWF model, with correlations > 0.92 for 1-month-lead predictions and >0.65 for 6-month-lead predictions in each month (Fig. 7). This forecast quality is consistent with the high autocorrelation (or persistence) of the Niño index (Fig. S16), indicating that the persistence of ENSO is possibly one reason for its high forecast quality. Long-lead forecasts of northerly moisture transport associated with SALLJ (represented by the V850 index) in October–December and easterly moisture transport associated with trade winds (represented by the U850 index) in March also have high correlation with observations (Fig. 7), which is consistent with the high correlation between the indices and the lead-time Niño index in corresponding months (Fig. S16), indicating that the prediction skill of the V850 during October–December and that of U850 in March are highly correlated with the ENSO signal at least 6 months before. However, the forecasts of V850 and U850 in other months do not agree with observations except when the predictions were made with a short lead time (e.g., 1 month). The indices in those months (except for U850 in November and December) are not correlated with the 1-month-lead Niño index (Fig. S16), demonstrating that the predictability of V850 and U850 in those months is not related to Niño-3.4, indicating the independence of the northerly moisture transport associated with SALLJ and the easterly moisture transport associated with trade winds from the ENSO signal in those months.

Figure 8 shows the performance of the ECMWF model in capturing the linkages between the circulation patterns and the climate variable January VPD. The spatial map of the January VPD is grouped into three clusters (Fig. 8a). Each cluster represents a region where the January VPD is strongly correlated with one or more of the patterns/indices: cluster 1 is correlated with the U850 and V850 indices, cluster 2 with Niño-3.4, and cluster 3 with V850 (Fig. 8b). For the pixels whose VPD is correlated with Niño-3.4 (cluster 2, red dots in Fig. 8), the forecast correlations between VPD and Niño-3.4 agree with the observed correlations in spite of slight overestimations with longer lead times (Fig. 8c); the VPD forecasts also agree with observations ($r > 0.53$; $p < 0.01$), with slightly decreases in correlation with longer lead times (Fig. 8d). For the pixels that are correlated with U850 (cluster 1, blue dots in Fig. 8) (which are also correlated with V850), the model captures the correlation between VPD and U850, but overestimates the correlation between VPD and Niño-3.4 with lead times longer than 2 months (Fig. 8c). The Niño-3.4 index is well predicted, but the relationship between Niño-3.4 and VPD is wrong, and the wrong relationship could be the reason for the incorrect estimates of VPD (Fig. 8d). For the pixels

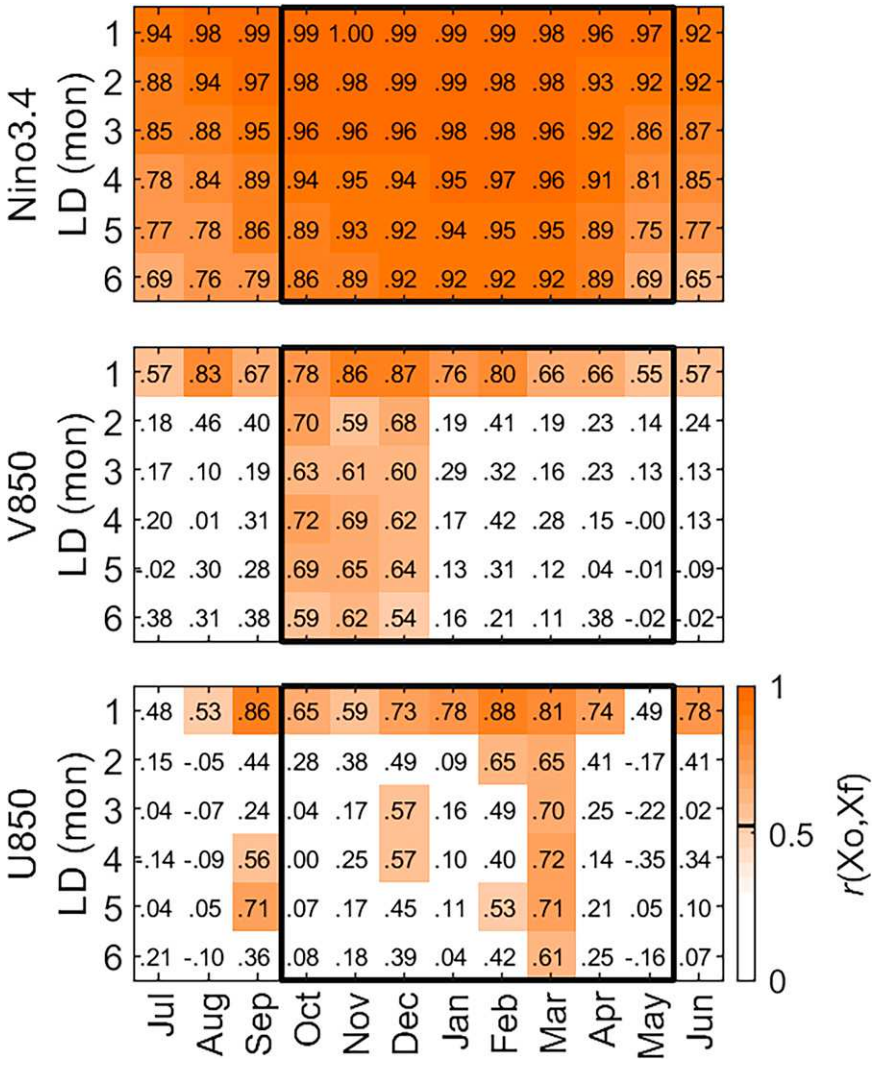


FIG. 7. The correlation coefficients between observed and forecasted indices (Niño-3.4, V850, and U850) (as in step 3 in Fig. 2) in each month with each lead time from ECMWF. The CCs are calculated from the times series between 1994 and 2016 and those that are significant at 99% confidence level via two-sided Student's $t$ test are colored and marked in the color bar. The growing season from October to May is boxed.

that are correlated with V850 (cluster 3, orange dots in Fig. 8), the correlation between VPD and V850 is well captured by the model with the 1-month lead time but is overestimated with longer lead times (Fig. 8d).

Figure 8d also shows that the performance of VPD forecasts is consistent with the correlation between VPD and Niño-3.4 when the lead time is longer than 2 months, indicating that the forecast skill of VPD in the study domain with long lead times is possibly linked to Niño-3.4, even if the regions are not significantly affected by Niño-3.4. In other words, for regions that are affected by ENSO, the forecasts of January VPD are well predicted, but for regions that are not affected by ENSO, the forecasts of January VPD are not well predicted in the ECMWF model. This model deficiency is found for other climate variables (temperature and precipitation) and in other months as well (supplemental videos S1, S2, and S3). To quantify the attribution of the circulation pattern errors to climate variable errors in regions that are significantly affected by the circulation pattern, we show the $r^2$ metric between those two errors in Fig. 9. Figure 9 reveals that although the impact area of Niño-3.4 on the three climate variables is greater than 20% of the total area of the study domain for some months in the growing season, the Niño-3.4 errors explains less than 10% of the variance of the errors of variables in the affected areas for almost all months. The U850 and V850 have larger impact areas than Niño-3.4, especially for precipitation and VPD, and the errors in U850 and V850 explain much more

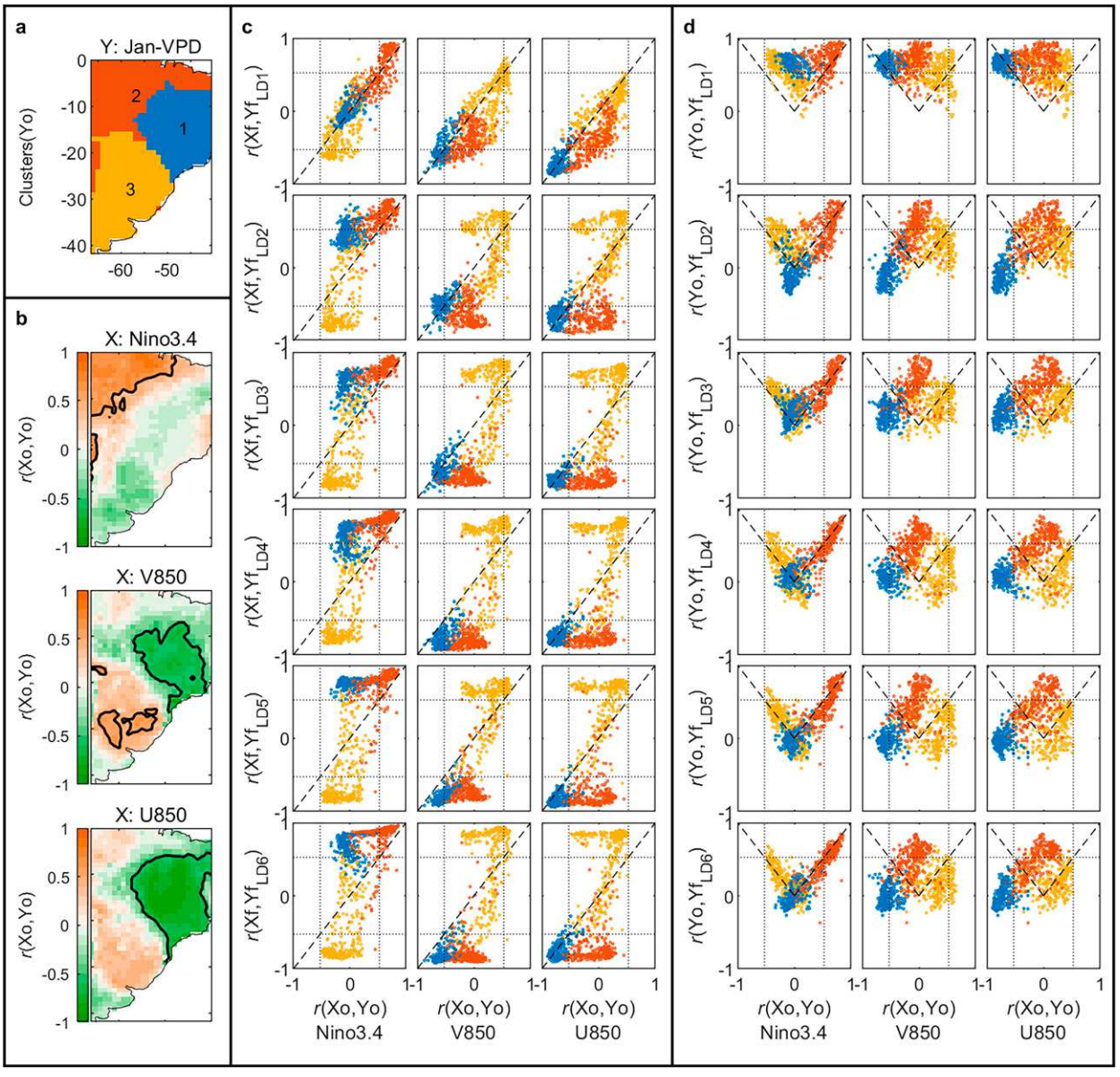


FIG. 8. The relationship between January VPD and the three indices (Niño-3.4, V850, U850) for each pixel grouped via clustering analysis. (a) The clusters of each pixel based on the observation of January VPD between 1994 and 2016. (b) The observed correlation between VPD and the three indices [$r$(Xo, Yo)]. Thick black lines indicate the 99% confidence level via two-sided Student's $t$ test. (c) The scatterplot of observed [$r$(Xo, Yo)] vs forecast [$r$(Xf, Yf)] correlation between VPD and the three indices in six lead times (LD1–6 months). The dotted lines indicate the 99% confidence level for the correlation coefficients, and the dashed lines are the diagonals. Scatters on the diagonal lines indicate that the model perfectly captures the relationship between the index and VPD, those above/below the diagonal lines indicate that the model overestimates/underestimates the positive relationship or underestimates/overestimates the negative relationship. (d) The scatterplot of the observed correlation between VPD and the three indices [$r$(Xo, Yo)] vs forecast skill of VPD in each lead time (LD1–6 months) measured by the correlation between observed and forecasted VPD [$r$(Yo, Yf)]. The dotted lines indicate the 99% confidence level for the correlation coefficients, the dashed lines are the diagonals, and the negative parts for $r$(Yo, Yf) are omitted due to meaninglessness. Scatters along the diagonals indicate that the prediction skill of the variable from the dynamical model is equivalent to the statistical impact from the index; above the diagonal lines means that the prediction from the dynamical model is better than the statistical impact from the index and vice versa.

variance than the errors in Niño-3.4 for all variables in all months. The errors in U850, for example, explain 78%, 72%, and 59% variance of the errors of January VPD, temperature, and precipitation of the impacted areas, respectively.

## 4. Summary

As seasonal climate forecasts are playing an increasing importance for socioeconomic applications, the quality of those forecasts needs to be evaluated prior to their uses. This study

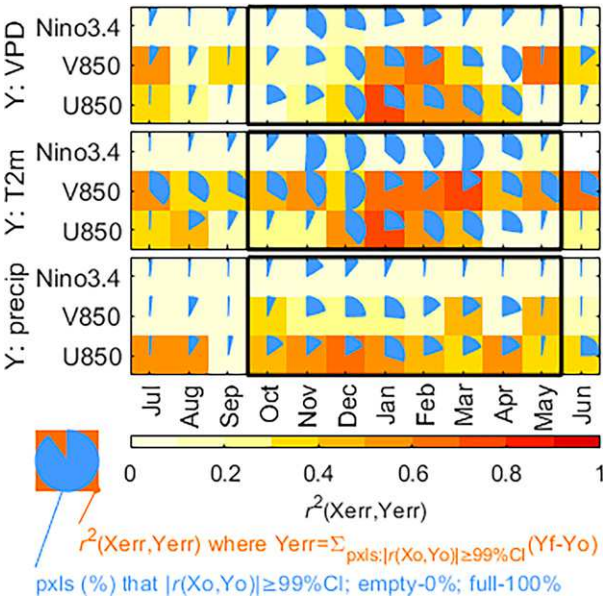


FIG. 9. The $r^2$ metric between climate variable prediction errors (Yerr) and index prediction errors (Xerr) [$r^2$(Xerr, Yerr)]. The $r^2$ are calculated using samples from all hindcast years (1994–2016) and all lead times (1–6 months) for the predictions of each month. The climate variable prediction errors are the averaged errors from all pixels whose climate variable is significantly correlated (99% confidence level) with the index based on observations, and the percentage of pixels included against all pixels in the study domain are shown with a blue circular sector, with an empty circle representing 0%, and a full circle representing 100% pixels.

evaluated monthly forecasts of three socioeconomically important variables (temperature, precipitation, and VPD) from five operational dynamical models. Focused on the major cropland areas over South America, we showed that the forecasts are better in the growing-season months (October–May) than in non-growing-season months (June–September) and the quality of forecasts decreases with longer lead times; those variations of the forecast performance are consistent with previous studies (Andrian et al. 2023).

The ECMWF model provides the best forecasts among the models evaluated. Similar to previous studies (Bombardi et al. 2018; Andrian et al. 2023), we found spatial variations for the quality of the forecasts from the ECMWF model. Specifically, temperature forecasts have the highest quality among the three variables evaluated, with high quality over northern South America even for 6-month-lead predictions, but low quality over southern South America when the lead time exceeds 2 months. Precipitation forecasts are the worst among the three climate variables, but they are of high quality over the regions of Uruguay and eastern Argentina in November and December even with a 6-month lead time. The VPD forecasts are also of high quality over northeastern Brazil and over the region of Uruguay and eastern Argentina in the growing season, for 6-month-lead predictions. Such long-lead predictions in the early growing season over the dense cropland and grassland regions could help support operational decisions on crop management, such as selection of crops and timing of planting.

The quality of the forecasts degrades significantly with longer lead times. To identify model deficiency and provide information for future model improvement, we evaluated the performance of the climate variables in relation to the performance of the circulation patterns that affect the local climate, specifically, ENSO, easterly moisture transport associated with trade winds, and northerly moisture transport associated with SALLJ. The ECMWF model captures the ENSO signal well throughout the year with any lead times between 1 and 6 months, while the two local patterns are not forecasted as good as the ENSO signal. The model successfully predicted the impacts of ENSO on the local climate over regions affected by ENSO but overestimates the influence of ENSO over regions not affected by ENSO, leading to high performance of climate forecasts over regions affected by ENSO and low performance over regions not affected by ENSO. Error contribution analyses further identified that the forecast errors in local patterns explain more than half of the variance of the forecast errors in the climate variables, suggesting the necessity of improving the forecasts of local patterns for better seasonal climate forecasts.

*Acknowledgments.* The authors acknowledge financial support from Agroecosystem Sustainability Center (ASC) from University of Illinois Urbana–Champaign. K.G. also acknowledges the NSF CAREER Award. R.F. acknowledges the NSF (Award 1917781). The authors declare no conflict of interest.

*Data availability statement.* ERA5 monthly and hourly data from 1981 to present are available at https://doi.org/10.24381/cds.68d2bb30 and https://doi.org/10.24381/cds.e2161bac, respectively. CPC Global Unified Gauge-Based Analysis of Daily Precipitation data provided by the NOAA PSL, Boulder, Colorado, are available from their website at https://psl.noaa.gov. The Niño-3.4 index is downloaded from https://psl.noaa.gov/data/climateindices/list/. Forecast data for the five dynamical models are available at https://cds.climate.copernicus.eu, the monthly data on single levels and on pressure levels are downloaded from https://doi.org/10.24381/cds.68dd14c3 and https://doi.org/10.24381/cds.50ed0a73, respectively.

## REFERENCES

Allen, R. G., L. S. Pereira, D. Raes, and M. Smith, 1998: Crop evapotranspiration: Guidelines for computing crop water requirements. FAO Irrigation and Drainage Paper 56, 300 pp., https://www.fao.org/3/X0490E/X0490E00.htm.

Andersson, L., J. Wilk, L. P. Graham, J. Wikner, S. Mokwatlo, and B. Petja, 2020: Local early warning systems for drought–Could they add value to nationally disseminated seasonal climate forecasts? *Wea. Climate Extremes*, **28**, 100241, https://doi.org/10.1016/j.wace.2019.100241.

Andrian, L. G., M. Osman, and C. S. Vera, 2023: Climate predictability on seasonal timescales over South America from the NMME models. *Climate Dyn.*, https://doi.org/10.1007/s00382-022-06506-8, in press.

Boers, N., A. Rheinwalt, B. Bookhagen, H. M. J. Barbosa, N. Marwan, J. Marengo, and J. Kurths, 2014: The South American rainfall dipole: A complex network analysis of extreme events. *Geophys. Res. Lett.*, **41**, 7397–7405, https://doi.org/10.1002/2014GL061829.

Bombardi, R. J., L. Trenary, K. Pegion, B. Cash, T. DelSole, and J. L. Kinter III, 2018: Seasonal predictability of summer rainfall over South America. *J. Climate*, **31**, 8181–8195, https://doi.org/10.1175/JCLI-D-18-0191.1.

Cai, W., and Coauthors, 2020: Climate impacts of the El Niño–Southern Oscillation on South America. *Nat. Rev. Earth Environ.*, **1**, 215–231, https://doi.org/10.1038/s43017-020-0040-3.

Calì Quaglia, F., S. Terzago, and J. von Hardenberg, 2022: Temperature and precipitation seasonal forecasts over the Mediterranean region: Added value compared to simple forecasting methods. *Climate Dyn.*, **58**, 2167–2191, https://doi.org/10.1007/s00382-021-05895-6.

Ceglar, A., and A. Toreti, 2021: Seasonal climate forecast can inform the European agricultural sector well in advance of harvesting. *npj Climate Atmos. Sci.*, **4**, 42, https://doi.org/10.1038/s41612-021-00198-3.

Chan, S. C., S. K. Behera, and T. Yamagata, 2008: Indian Ocean dipole influence on South American rainfall. *Geophys. Res. Lett.*, **35**, L14S12, https://doi.org/10.1029/2008GL034204.

Clements, J., A. Ray, and G. Anderson, 2013: The value of Climate Services across economic and public sectors: A review of relevant literature. USAID Tech. Rep., 54 pp., https://www.climate-services.org/wp-content/uploads/2015/09/CCRD-Climate-Services-Value-Report_FINAL.pdf.

Colussi, J., and G. Schnitkey, 2021: Brazil likely to remain world leader in soybean production. Farmdoc Daily, 12 July, https://farmdocdaily.illinois.edu/2021/07/brazil-likely-to-remain-world-leader-in-soybean-production.html.

Ehsan, M. A., and Coauthors, 2021: Seasonal predictability of Ethiopian Kiremt rainfall and forecast skill of ECMWF's SEAS5 model. *Climate Dyn.*, **57**, 3075–3091, https://doi.org/10.1007/s00382-021-05855-0.

ESA, 2010: GLOBCOVER 2009: Products description and validation report. ESA, 53 pp., http://due.esrin.esa.int/page_globcover.php.

FAO, 2021: World food and agriculture–Statistical yearbook 2021. FAO Rep., 368 pp., https://doi.org/10.4060/cb4477en.

Ferreira, G. W. S., M. S. Reboita, and A. Drumond, 2022: Evaluation of ECMWF-SEAS5 seasonal temperature and precipitation predictions over South America. *Climate*, **10**, 128, https://doi.org/10.3390/cli10090128.

Ghil, M., and K. Mo, 1991: Intraseasonal oscillations in the global atmosphere. Part II: Southern Hemisphere. *J. Atmos. Sci.*, **48**, 780–790, https://doi.org/10.1175/1520-0469(1991)048<0780:IOITGA>2.0.CO;2.

Gill, A. E., 1980: Some simple solutions for heat-induced tropical circulation. *Quart. J. Roy. Meteor. Soc.*, **106**, 447–462, https://doi.org/10.1002/qj.49710644905.

Gillett, N. P., T. D. Kell, and P. D. Jones, 2006: Regional climate impacts of the Southern Annular Mode. *Geophys. Res. Lett.*, **33**, L23704, https://doi.org/10.1029/2006GL027721.

Grossiord, C., T. N. Buckley, L. A. Cernusak, K. A. Novick, B. Poulter, R. T. W. Siegwolf, J. S. Sperry, and N. G. McDowell, 2020: Plant responses to rising vapor pressure deficit. *New Phytol.*, **226**, 1550–1566, https://doi.org/10.1111/nph.16485.

Gubler, S., and Coauthors, 2020: Assessment of ECMWF SEAS5 seasonal forecast performance over South America. *Wea. Forecasting*, **35**, 561–584, https://doi.org/10.1175/WAF-D-19-0106.1.

Hao, Z., F. Hao, V. P. Singh, and X. Zhang, 2018: Quantifying the relationship between compound dry and hot events and El Niño–Southern Oscillation (ENSO) at the global scale. *J. Hydrol.*, **567**, 332–338, https://doi.org/10.1016/j.jhydrol.2018.10.022.

Irving, D., and I. Simmonds, 2016: A new method for identifying the Pacific–South American pattern and its influence on regional climate variability. *J. Climate*, **29**, 6109–6125, https://doi.org/10.1175/JCLI-D-15-0843.1.

Jia, L., and Coauthors, 2015: Improved seasonal prediction of temperature and precipitation over land in a high-resolution GFDL climate model. *J. Climate*, **28**, 2044–2062, https://doi.org/10.1175/JCLI-D-14-00112.1.

Johnson, S. J., and Coauthors, 2019: SEAS5: The new ECMWF seasonal forecast system. *Geosci. Model Dev.*, **12**, 1087–1117, https://doi.org/10.5194/gmd-12-1087-2019.

Kimm, H., K. Guan, P. Gentine, J. Wu, C. J. Bernacchi, B. N. Sulman, T. J. Griffis, and C. Lin, 2020: Redefining droughts for the U.S. Corn Belt: The dominant role of atmospheric vapor pressure deficit over soil moisture in regulating stomatal behavior of Maize and Soybean. *Agric. For. Meteor.*, **287**, 107930, https://doi.org/10.1016/j.agrformet.2020.107930.

Klingaman, N. P., and Coauthors, 2021: Subseasonal prediction performance for austral summer South American rainfall. *Wea. Forecasting*, **36**, 147–169, https://doi.org/10.1175/WAF-D-19-0203.1.

Lobell, D. B., M. J. Roberts, W. Schlenker, N. Braun, B. B. Little, R. M. Rejesus, and G. L. Hammer, 2014: Greater sensitivity to drought accompanies maize yield increase in the U.S Midwest. *Science*, **344**, 516–519, https://doi.org/10.1126/science.1251423.

Manzanas, R., M. D. Frías, A. S. Cofiño, and J. M. Gutiérrez, 2014: Validation of 40 year multimodel seasonal precipitation forecasts: The role of ENSO on the global skill. *J. Geophys. Res. Atmos.*, **119**, 1708–1719, https://doi.org/10.1002/2013JD020680.

Montini, T. L., C. Jones, and L. M. V. Carvalho, 2019: The South American low-level jet: A new climatology, variability, and changes. *J. Geophys. Res. Atmos.*, **124**, 1200–1218, https://doi.org/10.1029/2018JD029634.

Mueller, S. E., A. E. Thode, E. Q. Margolis, L. L. Yocom, J. D. Young, and J. M. Iniguez, 2020: Climate relationships with increasing wildfire in the southwestern US from 1984 to 2015. *For. Ecol. Manage.*, **460**, 117861, https://doi.org/10.1016/j.foreco.2019.117861.

Muñoz Sabater, J., 2019a: ERA5-Land hourly data from 1981 to present. Copernicus Climate Change Service (C3S) Climate Data Store (CDS), accessed 5 August 2022, https://doi.org/10.24381/cds.e2161bac.

——, 2019b: ERA5-Land monthly averaged data from 1981 to present. Copernicus Climate Change Service (C3S) Climate Data Store (CDS), accessed 5 August 2022, https://doi.org/10.24381/cds.68d2bb30.

National Research Council, 2016: Enhancing the value and benefits of S2S forecasts. *Next Generation Earth System Prediction: Strategies for Subseasonal to Seasonal Forecasts*, The National Academies Press, 43–82, https://doi.org/10.17226/21873.

Ogutu, G. E. O., W. H. P. Franssen, I. Supit, P. Omondi, and R. W. A. Hutjes, 2017: Skill of ECMWF system-4 ensemble seasonal climate forecasts for East Africa. *Int. J. Climatol.*, **37**, 2734–2756, https://doi.org/10.1002/joc.4876.

Orlov, A., J. Sillmann, and I. Vigo, 2020: Better seasonal forecasts for the renewable energy industry. *Nat. Energy*, **5**, 108–110, https://doi.org/10.1038/s41560-020-0561-5.

Peng, B., K. Guan, M. Pan, and Y. Li, 2018: Benefits of seasonal climate prediction and satellite data for forecasting U.S. maize yield. *Geophys. Res. Lett.*, **45**, 9662–9671, https://doi.org/10.1029/2018GL079291.

Pepler, A. S., L. B. Díaz, C. Prodhomme, F. J. Doblas-Reyes, and A. Kumar, 2015: The ability of a multi-model seasonal forecasting ensemble to forecast the frequency of warm, cold and wet extremes. *Wea. Climate Extremes*, **9**, 68–77, https://doi.org/10.1016/j.wace.2015.06.005.

Prein, A. F., E. Towler, M. Ge, D. Llewellyn, S. Baker, S. Tighi, and L. Barrett, 2022: Sub-seasonal predictability of North American monsoon precipitation. *Geophys. Res. Lett.*, **49**, e2021GL095602, https://doi.org/10.1029/2021GL095602.

Rattis, L., and Coauthors, 2021: Climatic limit for agriculture in Brazil. *Nat. Climate Change*, **11**, 1098–1104, https://doi.org/10.1038/s41558-021-01214-3.

Salio, P., M. Nicolini, and E. J. Zipser, 2007: Mesoscale convective systems over southeastern South America and their relationship with the South American low-level jet. *Mon. Wea. Rev.*, **135**, 1290–1309, https://doi.org/10.1175/MWR3305.1.

Thomson, M. C., F. J. Doblas-Reyes, S. J. Mason, R. Hagedorn, S. J. Connor, T. Phindela, A. P. Morse, and T. N. Palmer, 2006: Malaria early warnings based on seasonal climate forecasts from multi-model ensembles. *Nature*, **439**, 576–579, https://doi.org/10.1038/nature04503.

Vera, C. S., and M. Osman, 2018: Activity of the Southern Annular Mode during 2015–2016 El Niño event and its impact on Southern Hemisphere climate anomalies. *Int. J. Climatol.*, **38**, e1288–e1295, https://doi.org/10.1002/joc.5419.

Voelker, S. L., F. C. Meinzer, B. Lachenbruch, J. R. Brooks, and R. P. Guyette, 2014: Drivers of radial growth and carbon isotope discrimination of bur oak (*Quercus macrocarpa Michx.*) across continental gradients in precipitation, vapour pressure deficit and irradiance. *Plant Cell Environ.*, **37**, 766–779, https://doi.org/10.1111/pce.12196.

Wang, H., R. Fu, W. Tan, and W. T. Liu, 2004: Influence of cross-Andes flow on the SALLJs and application of real-time scatterometer observations to forecasting the SALLJs. *CLIVAR Exchanges*, No. 29, International CLIVAR Project Office, Southampton, United Kingdom, 3 pp., https://www.cpc.ncep.noaa.gov/products/people/hwang/pdf/N_2004_Wang_Exchanges.pdf.

Ward, J. H., 1963: Hierarchical grouping to optimize an objective function. *J. Amer. Stat. Assoc.*, **58**, 236–244, https://doi.org/10.1080/01621459.1963.10500845.

White, C. J., and Coauthors, 2022: Advances in the application and utility of subseasonal-to-seasonal predictions. *Bull. Amer. Meteor. Soc.*, **103**, E1448–E1472, https://doi.org/10.1175/BAMS-D-20-0224.1.

Yin, L., R. Fu, Y.-F. Zhang, P. A. Arias, D. N. Fernando, W. Li, K. Fernandes, and A. R. Bowerman, 2014: What controls the interannual variation of the wet season onsets over the Amazon? *J. Geophys. Res. Atmos.*, **119**, 2314–2328, https://doi.org/10.1002/2013JD021349.

Yuan, W., and Coauthors, 2019: Increased atmospheric vapor pressure deficit reduces global vegetation growth. *Sci. Adv.*, **5**, eaax1396, https://doi.org/10.1126/sciadv.aax1396.

Zhang, J., and Coauthors, 2021a: Assessing different plant-centric water stress metrics for irrigation efficacy using soil-plant-atmosphere-continuum simulation. *Water Resour. Res.*, **57**, e2021WR030211, https://doi.org/10.1029/2021WR030211.

——, and Coauthors, 2021b: Sustainable irrigation based on co-regulation of soil water supply and atmospheric evaporative demand. *Nat. Commun.*, **12**, 5549, https://doi.org/10.1038/s41467-021-25254-7.

Zhao, S., Y. Deng, and R. X. Black, 2017: A dynamical and statistical characterization of U.S. extreme precipitation events and their associated large-scale meteorological patterns. *J. Climate*, **30**, 1307–1326, https://doi.org/10.1175/JCLI-D-15-0910.1.

——, R. Fu, Y. Zhuang, and G. Wang, 2021: Long-lead seasonal prediction of streamflow over the Upper Colorado River Basin: The role of the Pacific Sea surface temperature and beyond. *J. Climate*, **34**, 6855–6873, https://doi.org/10.1175/JCLI-D-20-0824.1.

——, and Coauthors, 2023: Extended seasonal prediction of spring precipitation over the Upper Colorado River Basin. *Climate Dyn.*, **60**, 1815–1829, 3https://doi.org/10.1007/s00382-022-06422-x.

Zhou, W., and Coauthors, 2020: Connections between the hydrological cycle and crop yield in the rainfed U.S. Corn Belt. *J. Hydrol.*, **590**, 125398, https://doi.org/10.1016/j.jhydrol.2020.125398.

Zhuang, Y., R. Fu, B. D. Santer, R. E. Dickinson, and A. Hall, 2021: Quantifying contributions of natural variability and anthropogenic forcings on increased fire weather risk over the western United States. *Proc. Natl. Acad. Sci. USA*, **118**, e2111875118, https://doi.org/10.1073/pnas.2111875118.

Ziervogel, G., M. Bithell, R. Washington, and T. Downing, 2005: Agent-based social simulation: A method for assessing the impact of seasonal climate forecast applications among smallholder farmers. *Agric. Syst.*, **83** (1), 1–26, https://doi.org/10.1016/j.agsy.2004.02.009.